Optics Letters

Giant spin-selective asymmetric transmission in multipolar-modulated metasurfaces

Dina Ma,[1] Zhancheng Li,[1] Yuebian Zhang,[1] Wenwei Liu,[1] Hua Cheng,[1] Shuqi Chen,[1,2,3,*] and Jianguo Tian[1]

[1]The Key Laboratory of Weak Light Nonlinear Photonics, Ministry of Education, School of Physics and Teda Applied Physics Institute, Nankai University, Tianjin 300071, China
[2]Renewable Energy Conversion and Storage Center, Nankai University, Tianjin 300071, China
[3]The Collaborative Innovation Center of Extreme Optics, Shanxi University, Taiyuan, Shanxi 030006, China
*Corresponding author: schen@nankai.edu.cn

Received 28 May 2019; revised 26 June 2019; accepted 30 June 2019; posted 1 July 2019 (Doc. ID 367882); published 25 July 2019

Spin-selective manipulation of optical waves is widely utilized in various optical techniques and plays a key role in modern nanophotonics. While numerous efficient approaches have been applied in metasurfaces to realize spin-selective manipulation of optical waves, the implementation of giant spin-selective asymmetric transmission remains a challenge. Here, we propose an all-dielectric metasurface to realize giant tri-band spin-selective asymmetric transmission in the near infrared regime. The proposed giant spin-selective asymmetric transmission is attributed to the excitation of overlapping multipolar resonances in the dielectric elliptic cylinders, which can be well manipulated by changing the structure parameters. This research demonstrates the great potential of all-dielectric metasurfaces for spin-selective transmission manipulation, which provide helpful insights and intriguing possibilities for applications in information optics, quantum optics, optical sensing, and imaging.

https://doi.org/10.1364/OL.44.003805

Harnessing light for modern nanophotonics applications often involves the spin-selective manipulation of optical waves. With great precision and exceptional capabilities for both single-dimensional and multidimensional manipulation of optical waves, metasurfaces have emerged as an appealing alternative to realize giant spin-selective manipulation of optical waves, which have attracted wide interest among the scientific community in recent years [1–3]. Recent advances in metasurfaces prove that the implementation of spin-selective manipulation of optical waves has a great impact in the areas of quantum optics, information optics, optical sensing, and imaging [4–11]. Although numerous efficient approaches have been applied in metasurfaces to realize spin-selective manipulation of optical waves, the implementation of giant spin-selective asymmetric transmission remains a challenge.

Spin-selective asymmetric transmission, which is associated with circular conversion dichroism, can be widely used for the realization of asymmetric optical filters, optical sensing, chiral imaging, and optical anticounterfeiting [5,7,9]. However, the implementations of spin-selective asymmetric transmission in metasurfaces are always with low efficiency, which prevents them from the real applications [12–15]. One way to overcome this drawback is utilizing tapered metallic gratings or a few-layer design, in which the interaction between nanostructures and optical waves can be significantly enhanced [16–22]. For example, Liu *et al.* demonstrated a giant mutual dual-band spin-selective asymmetric transmission by utilizing few-layer anisotropic metasurfaces [21]. However, this approach is not an appealing alternative due to its complex structure design and time-consuming top-down fabrication process. The other way to improve the efficiency of spin-selective asymmetric transmission in metasurfaces is utilizing all-dielectric nanostructures [23–26]. For example, Zhang *et al.* experimentally realized a giant and broadband spin-selective asymmetric transmission based on asymmetric photonic spin-orbit interaction in all-dielectric metasurfaces [25]. The implementations of giant spin-selective asymmetric transmission in these all-dielectric approaches are either in a broadband or in a single narrow band, so giant multiband spin-selective asymmetric transmission in all-dielectric metasurfaces is yet to be presented. Moreover, the spin-selective asymmetric transmissions in these approaches are based on either asymmetric photonic spin-orbit interaction or a single resonance mode; the realization of giant spin-selective asymmetric transmission based on the overlapping of multipolar resonances in all-dielectric metasurfaces still needs to be validated.

Here, we demonstrate the use of an all-dielectric anisotropic metasurface for the implementation of giant tri-band spin-selective asymmetric transmission in the near infrared wave band. The proposed all-dielectric metasurface can realize giant spin-selective asymmetric transmission with peak values of −0.83, −0.68, and 0.94 at wavelengths of 997 nm, 1042 nm, and 1055 nm, respectively. By decomposing the multipolar modes of scattering cross-sections, we prove that the proposed giant tri-band spin-selective asymmetric transmission is attributed to the excitation of overlapping multipolar resonances in

the dielectric elliptic cylinders. We further show that the excitation of overlapping multipolar resonances in the dielectric elliptic cylinders can be well manipulated by changing the structure parameters of the dielectric elliptic cylinders, resulting in the variation of the spin-selective asymmetric transmission. The demonstration of giant tri-band spin-selective asymmetric transmission, which is based on the effective modulation of multipolar resonances in all-dielectric metasurfaces, opens new routes for real applications in asymmetric optical filters, optical encryption, and so forth.

A schematic of the designed all-dielectric metasurface is shown in Fig. 1. The proposed design, which is on a SiO_2 substrate, consists of two amorphous Si nanoelliptical cylinders with sizes $a_1 = 150$ nm, $a_2 = 140$ nm, $b_1 = 90$ nm, $b_2 = 50$ nm, and $h = 700$ nm. The long axes of two nanoelliptical are along the y axis and 45 deg from the y axis, respectively. The distance d between two nanoelliptical cylinders is equal to 300 nm, and the periods of the unit cell along the x and y axes are $P_x = 600$ nm and $P_y = 500$ nm, respectively. The finite element method (COMSOL Multiphysics) had been used to simulate, analyze, and explore the characterizations of the designed metasurface. The SiO_2 substrate is regarded as a lossless material with a refractive index equal to 1.5. The optical constants of amorphous Si were taken from Ref. [27]. Periodic boundary conditions were applied in both the x and y directions of the unit cell, and perfectly matched layers were placed in the z direction. The overall structure was illuminated by circular-polarized plane waves propagating along the z axis. In our theoretical analysis, the $+z$ and $-z$ directions were defined as the forward and backward directions of propagation, respectively.

First, the realization condition of giant spin-selective asymmetric transmission in metasurfaces is theoretically analyzed by utilizing advanced Jones calculus [28,29]. For circular-polarized incident waves, the generally complex amplitudes of the incident field and the transmitted field can be related by Jones matrix $\mathbf{T}$:

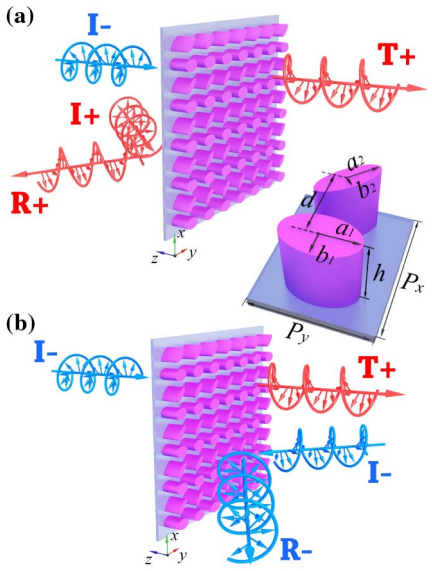

Fig. 1. Artistic rendering of the spin-selective asymmetric transmission in the proposed all-dielectric metasurface. (a) Spin-selective transmission and (b) asymmetric transmission for incident waves with a constant spin propagating along two opposite directions.

$$\begin{pmatrix} T_+ \\ T_- \end{pmatrix} = \mathbf{T}^f_{\text{circ}} \begin{pmatrix} I_+ \\ I_- \end{pmatrix} = \begin{pmatrix} T_{++} & T_{+-} \\ T_{-+} & T_{--} \end{pmatrix} \begin{pmatrix} I_+ \\ I_- \end{pmatrix}. \quad (1)$$

Here, the subscript "circ" of $\mathbf{T}^f_{\text{circ}}$ indicates that the Jones matrix lies in the circular base, while the superscript "f" indicates the forward direction. The subscripts "+" and "−" indicate the spin of the optical waves and represent right-handed and left-handed circular polarization, respectively. The Jones matrix for the backward direction then can be obtained by applying the reciprocity theorem:

$$\mathbf{T}^b_{\text{circ}} = \begin{pmatrix} T_{++} & T_{-+} \\ T_{+-} & T_{--} \end{pmatrix}. \quad (2)$$

The giant spin-selective asymmetric transmission is associated with the circular conversion dichroism. For example, when the amplitude of circular conversion coefficient T_{+-} is much bigger than the other three transmission coefficients, we can treat the other three transmission coefficients as zero and obtain

$$t^f_+ = |T^f_+|^2 = |T_{+-}I_-|^2, \quad (3a)$$

$$t^f_- = |T^f_-|^2 = 0, \quad (3b)$$

$$t^b_+ = |T^b_+|^2 = 0, \quad (3c)$$

$$t^b_- = |T^b_-|^2 = |T_{+-}I_+|^2, \quad (3d)$$

where t^f_+, t^f_-, t^b_+, t^b_- represent the transmission intensity for optical waves with different spins propagating along the forward and backward directions, respectively. Equations (3a) and (3b) [or (3c) and (3d)] indicate the spin-selective transmission, as shown in Fig. 1(a), while Eqs. (3a) and (3c) [or (3b) and (3d)] indicate the asymmetric transmission, as shown in Fig. 1(b). Thus, the giant spin-selective asymmetric transmission can be realized when the amplitude of one of the circular conversion coefficients in the Jones matrix is much bigger than the other three transmission coefficients.

To quantitatively analyze the giant spin-selective asymmetric transmission in the proposed metasurface, we simulated the squared moduli $t_{ij} = |T_{ij}|^2$ of four transmission coefficients for the proposed design and calculated the asymmetric transmission parameter defined as $\Delta = |T_{-+}|^2 - |T_{+-}|^2$, as shown in Fig. 2. Simulated results indicate that the squared moduli of the circular conversion coefficient T_{-+} (or T_{+-}) is much larger than the other three transmission coefficients at 997 nm (P_1), 1042 nm (P_2), and 1055 nm (P_3), which result in giant spin-selective asymmetric transmission with asymmetric transmission parameters of −0.83, −0.68, and 0.94. According to Eq. (3), when the value of Δ is negative, the left-handed circular-polarized incident waves can pass through the designed metasurface in the forward direction, while the right-handed circular-polarized incident waves can pass through the designed metasurface in the backward direction. When the value of Δ is positive, the situation is inverted.

In order to understand the origin of the proposed giant spin-selective asymmetric transmission, we evaluated the optical response of the proposed design by analyzing the contribution of multipole resonances in dielectric nanostructures. Figures 3(a)–3(c) show the calculated results of scattering properties of the proposed metasurface at P_1, P_2, P_3 by decomposing the multipolar modes of scattering spectra based on the

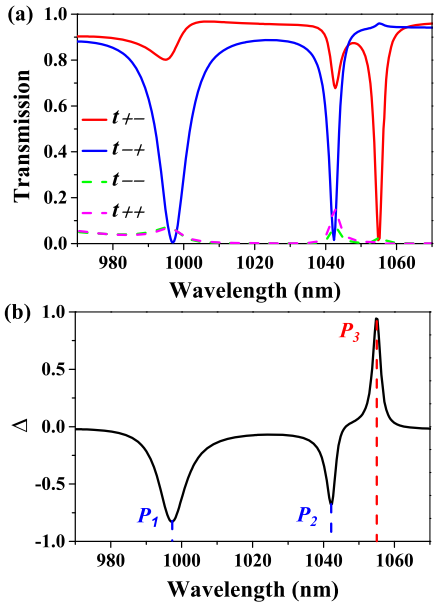

Fig. 2. (a) Simulated results of the squared moduli $t_{ij} = |T_{ij}|^2$ of four transmission coefficients of the proposed all-dielectric metasurfaces. (b) Calculated results of the asymmetric transmission parameter $\Delta = |T_{-+}|^2 - |T_{+-}|^2$.

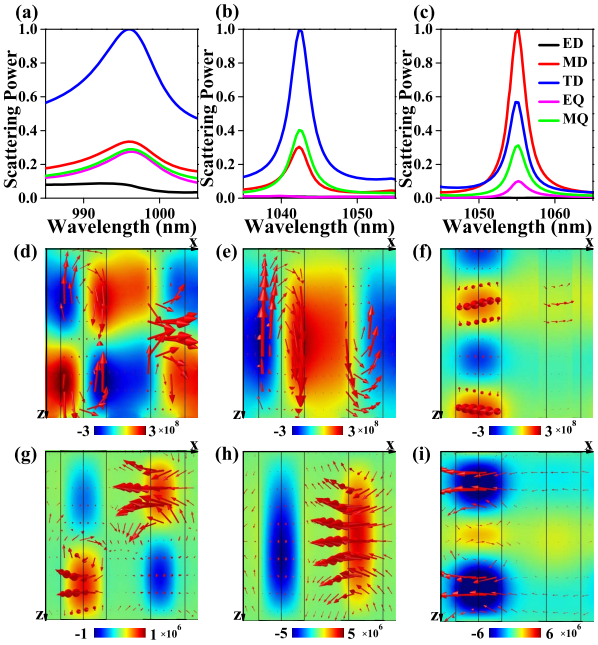

Fig. 3. Calculated results of multipolar decomposition of scattering spectra at (a) P_1 with right-handed circular-polarized incident waves, (b) P_2 with right-handed circular-polarized incident waves, and (c) P_3 with left-handed circular-polarized incident waves. The distribution of the current density (red arrows) and real part of electric field component (d) E_z in the $x-z$ plane at P_1, (e) E_z in the $x-z$ plane at P_2, (f) E_y in the $x-z$ plane at P_3. The direction of the magnetic field (red arrows) and the distribution of the real part of magnetic field component (g) H_y in the $x-z$ plane at P_1, (h) H_y in the $x-z$ plane at P_2, (i) H_x in the $x-z$ plane at P_3.

Cartesian multipole decomposition method [30–33]. The decomposition calculations indicate that electric dipole (ED), magnetic dipole (MD), toroidal dipole (TD), electric quadrupole (EQ), and magnetic quadrupole (MQ) are main resonances, which significantly contribute to the scattering property of the proposed metasurface. The realization of giant spin-selective asymmetric transmission at P_1 and P_2 is ascribed to the excitation and overlapping of multipole resonance modes when illuminating right-handed circular-polarized waves. As shown in Fig. 3(a), the giant spin-selective asymmetric transmission at P_1 is mainly attributed to the excitation and overlapping of the TD, MD, MQ, and EQ resonance modes, in which the TD and MD modes play a dominant role. The simulated electric field distribution of the E_z component and magnetic field distribution of the H_y component at P_1 in Figs. 3(d) and 3(g) further verified the excitation of the TD mode, which significantly enhances the reflection of right-handed circular-polarized waves and results in the giant spin-selective asymmetric transmission. Compared with the calculated results in Fig. 3(a), the giant spin-selective asymmetric transmission at P_2 is mainly ascribed to the excitation and overlapping of TD, MQ, and MD resonance modes, as shown in Fig. 3(b). The simulated electric field distribution of the E_z component and magnetic field distribution of the H_y component at P_2 further prove that the TD resonance mode plays a dominating role in the implementation of giant spin-selective asymmetric transmission at P_2, as shown in Figs. 3(e) and 3(h). On the contrary, the giant spin-selective asymmetric transmission at P_3 is attributed to the excitation and overlapping of MD, TD, MQ, and EQ resonance modes when illuminating left-handed circular-polarized waves. Figures 3(f) and 3(i) show the simulated electric field distribution of the E_y component and magnetic field distribution of the H_x component at P_3. The MD resonance mode can be well observed, which plays a dominating role in the realization of giant spin-selective asymmetric transmission at P_3.

For further understanding of the overlapping of multipole resonance modes, we analyzed the variation of the asymmetric transmission parameter and its peak position with the changing of structure parameters of the proposed design in Fig. 4. As shown in Figs. 4(a) and 4(d), P_3 has a significant red shift with the variation of the height h of the nanoelliptical cylinders. This is because the giant spin-selective asymmetric transmission at P_3 is mainly dominated by the MD resonance mode that has a close relation with the height of the nanoelliptical cylinders, as shown in Fig. 3(f). The positions of P_1, P_2, P_3 are constant with the changing of the distance d between two nanoelliptical cylinders, as shown in Figs. 4(b) and 4(e), which indicate that the excitation and overlapping of the multipolar resonance modes in the proposed metasurface are weakly affected by the variation of d in a certain range. On the other hand, a new peak of the asymmetric transmission parameter will appear with the decreasing of d, which is associated with the excitation and overlapping of new MD, MQ, and TD resonance modes with left-handed circular-polarized waves. We also analyzed the influence of the rotation angle θ of the nanoelliptical cylinder, whose long axis is 45 deg ($\theta = 45°$) from the y axis in our design. The simulated results in Figs. 4(c) and 4(f) show that the changing of the rotation angle θ will significantly affect the positions of P_1 and P_2, and P_2 has a more significant red shift. The excitation of TD has a strong dependence on θ.

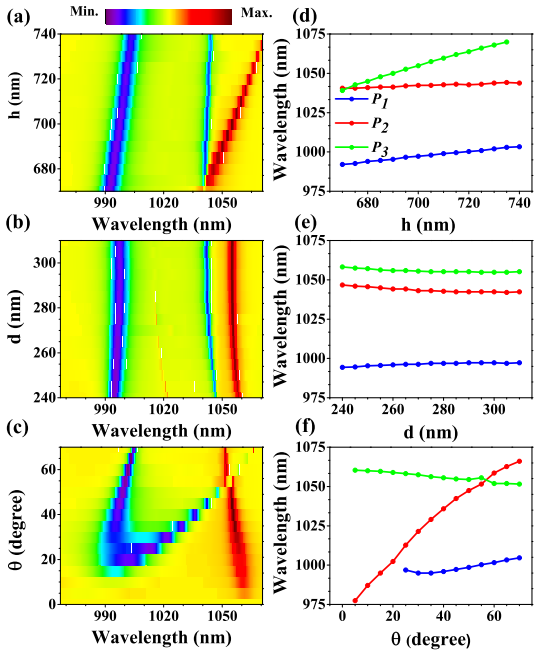

Fig. 4. Variation of (a)–(c) the asymmetric transmission parameter and (d)–(f) the peak position with the changing of (a), (d) the height h of the nanoelliptical cylinders, (b), (e) the distance d between two nanoelliptical cylinders, and (c), (f) the rotation angle θ of one nanoelliptical cylinder whose long axis is 45 deg from the y axis in our design.

When $\theta = 0°$, the excitation of multipole resonance modes with left-handed circular-polarized waves are the same as that with right-handed circular-polarized waves, so there is no giant spin-selective asymmetric transmission. The results in Fig. 4 allow us to manipulate the excitation and overlapping of the multipolar resonance modes in the proposed metasurface by changing the structure parameters of the nanoelliptical cylinders, resulting in the controlling of the giant spin-selective asymmetric transmission.

In conclusion, we present the theoretical analysis, design specifications, and simulated demonstration of an all-dielectric multipolar-modulated metasurface for the implementation of giant tri-band spin-selective asymmetric transmission in the near infrared wave band. The simulated results indicate that the giant spin-selective asymmetric transmission can be realized at three different wavelengths. The giant tri-band asymmetric transmission is attributed to the excitation of overlapping multipolar resonances in the dielectric elliptic cylinders, which has been well proved by decomposing the multipolar modes of scattering cross-sections and analyzing the variation of the working wave band with the changing of the structure parameters. The demonstration of giant tri-band spin-selective asymmetric transmission in the proposed multipolar-modulated metasurface plays an important role for further investigations of asymmetric transmission in an all-dielectric metasurface, which shall boost their applications in asymmetric optical filters, optical encryption, optical sensing, and so forth.

Funding. National Key Research and Development Program of China (2016YFA0301102, 2017YFA0303800); National Natural Science Foundation of China (NSFC) (11574163, 11774186, 91856101); Natural Science Foundation of Tianjin City for Distinguished Young Scientists (18JCJQJC45700); China Postdoctoral Science Foundation (2018M640224, 2018M640229); 111 Project (B07013).

REFERENCES

1. S. Chen, Z. Li, W. Liu, H. Cheng, and J. Tian, Adv. Mater. **31**, 1802458 (2019).
2. X. Luo, D. Tsai, M. Gu, and M. Hong, Adv. Opt. Photonics **10**, 757 (2018).
3. D. Neshev and I. Aharonovich, Light Sci. Appl. **7**, 58 (2018).
4. K. Wang, J. G. Titchener, S. S. Kruk, L. Xu, H. P. Chung, M. Parry, I. I. Kravchenko, Y.-H. Chen, A. S. Solntsev, Y. S. Kivshar, D. N. Neshev, and A. A. Sukhorukov, Science **361**, 1104 (2018).
5. Y. Zhang, Z. Li, W. Liu, Z. Li, H. Cheng, S. Chen, and J. Tian, Adv. Opt. Mater. **7**, 1801273 (2019).
6. Z. Li, W. Liu, Z. Li, C. Tang, H. Cheng, J. Li, X. Chen, S. Chen, and J. Tian, Laser Photon. Rev. **12**, 1800164 (2018).
7. Y. Zhao, A. N. Askarpour, L. Sun, J. Shi, X. Li, and A. Alú, Nat. Commun. **8**, 14180 (2017).
8. W. Li, Z. J. Coppens, L. V. Besteiro, W. Wang, A. O. Govorov, and J. Valentine, Nat. Commun. **6**, 8379 (2015).
9. M. Khorasaninejad, A. Ambrosio, P. Kanhaiya, and F. Capasso, Sci. Adv. **2**, e1501258 (2016).
10. J. B. Mueller, N. A. Rubin, R. C. Devlin, B. Groever, and F. Capasso, Phys. Rev. Lett. **118**, 113901 (2017).
11. L. Jin, Z. Dong, S. Mei, Y. F. Yu, Z. Wei, Z. Pan, and J. K. Yang, Nano Lett. **18**, 8016 (2018).
12. R. Singh, E. Plum, C. Menzel, C. Rockstuhl, A. K. Azad, R. A. Cheville, F. Lederer, W. Zhang, and N. I. Zheludev, Phys. Rev. B **80**, 153104 (2009).
13. E. Plum, V. A. Fedotov, and N. I. Zheludev, Appl. Phys. Lett. **94**, 131901 (2009).
14. Z. Li, W. Liu, H. Cheng, S. Chen, and J. Tian, Opt. Lett. **41**, 3142 (2016).
15. C. Pan, M. Ren, Q. Li, S. Fan, and J. Xu, Appl. Phys. Lett. **104**, 121112 (2014).
16. H. Cheng, Z. Liu, S. Chen, and J. Tian, Adv. Mater. **27**, 5410 (2015).
17. Z. Li, W. Liu, H. Cheng, J. Liu, S. Chen, and J. Tian, Sci. Rep. **6**, 35485 (2016).
18. Z. Li, W. Liu, H. Cheng, S. Chen, and J. Tian, Sci. Rep. **7**, 8204 (2017).
19. D. F. Tang, C. Wang, W. K. Pan, M. H. Li, and J. F. Dong, Opt. Express **25**, 11329 (2017).
20. N. Parappurath, F. Alpeggiani, L. Kuipers, and E. Verhagen, ACS Photon. **4**, 884 (2017).
21. J. Liu, Z. Li, W. Liu, H. Cheng, S. Chen, and J. Tian, Adv. Opt. Mater. **4**, 2028 (2016).
22. B. Tang, Z. Li, Z. Liu, F. Callewaert, and K. Aydin, Sci. Rep. **6**, 39166 (2016).
23. Z. Ma, Y. Li, Y. Li, Y. Gong, S. A. Maier, and M. Hong, Opt. Express **26**, 6067 (2018).
24. M. Kenney, S. Li, X. Zhang, X. Su, T. T. Kim, D. Wang, D. Wu, C. Ouyang, J. Han, W. Zhang, H. Sun, and S. Zhang, Adv. Mater. **28**, 9567 (2016).
25. F. Zhang, M. Pu, X. Li, P. Gao, X. Ma, J. Luo, H. Yu, and X. Luo, Adv. Funct. Mater. **27**, 1704295 (2017).
26. A. Ozer, N. Yilmaz, H. Kocer, and H. Kurt, J. Opt. **21**, 055104 (2019).
27. D. T. Pierce and W. E. Spicer, Phys. Rev. B **5**, 3017 (1972).
28. C. Menzel, C. Helgert, C. Rockstuhl, E. B. Kley, A. Tünnermann, T. Pertsch, and F. Lederer, Phys. Rev. Lett. **104**, 253902 (2010).
29. C. Menzel, C. Rockstuhl, and F. Lederer, Phys. Rev. A **82**, 053811 (2010).
30. T. Kaelberer, V. A. Fedotov, N. Papasimakis, D. P. Tsai, and N. I. Zheludev, Science **330**, 1510 (2010).
31. E. E. Radescu and G. Vaman, Phys. Rev. E **65**, 046609 (2002).
32. Z. Ma, S. M. Hanham, Y. Gong, and M. Hong, Opt. Lett. **43**, 911 (2018).
33. Y. Zhang, W. Liu, Z. Li, Z. Li, H. Cheng, S. Chen, and J. Tian, Opt. Lett. **43**, 1842 (2018).